This article has been accepted for publication in IEEE Photonics Journal. This is the author's version which has not been fully edited and content may change prior to final publication. Citation information: DOI 10.1109/JPHOT.2024.3467310

Visible To Near-Infrared Light Integrated Photonic Components On PECVD And LPCVD SiN Platform

Sen Yang, ZuoQin Ding, Xiao Li, Xiao Luo, ShuHua Zhai, XiuJun Zheng, Bo Wang, He Li, Zhuo Deng, QianShi Wang, Sarp Kerman, Chang Chen

***Abstract*—In this paper, we present our process design kits (PDKs) component performances for different wavelengths in the visible to near-infrared (VIS-NIR) range on Shanghai Industrial µTechnology Research Institute's (SITRI's) 200 mm Silicon Nitride (SiN) photonics platform. SiN waveguide platform has emerged as a promising technology due to its low optical loss, relatively high refractive index, and transparency across the VIS-NIR spectrum. The industrialization of SiN platforms requires matured PDKs. On SITRI's 200 mm SiN photonics platform, we developed PDKs using both Plasma-Enhanced Chemical Vapor Deposition (PECVD) and Low-Pressure Chemical Vapor Deposition (LPCVD) processes, with SiN layers of 180 nm and 150 nm thicknesses, respectively. The fabricated waveguides exhibit low propagation loss, ranging from 2.5 dB/cm to 0.34 dB/cm from 532 nm to 860 nm. Additionally, we present a low bending loss which is less than 0.06 dB/90° with a radius of 100 µm. Furthermore, the loss of the linear grating coupler is less than 2.6 dB at 785 nm. We have also achieved low-loss splitters, including 1×2 multimode interference (MMI) coupler, and directional coupler (DC), with a minimum excess loss of 0.03 dB. Additionally, micro ring resonators with high quality (Q) factors of 146,000 have been demonstrated. Our work on developing this PDK will open new opportunities for researchers and developers to design and fabricate advanced photonic devices on the SiN platform in SITRI's 200 mm fabrication line.**

***Index Terms*—Photonic integration, silicon nitride, process design kits, visible to near-infrared.**

This work was supported in part by the National Key Research and Development Program under Grant 2022YFE0107400 and 2021YFB3202500 and GuangCi Deep Mind Project of Ruijin Hospital-Shanghai Jiao Tong University School of Medicine. *(Corresponding author: Sarp Kerman and Chang Chen; Co-first authors: Sen Yang, ZuoQin Ding, Xiao Li).*

Sen Yang is with School of Microelectronics, Shanghai University, Shanghai, 201800, China, Shanghai Photonic View, Shanghai, 201900, China and Shanghai Industrial µTechnology Research Institute (SITRI), Shanghai, 201800, China(email: ysyang@shu.edu.cn).

ZuoQin Ding, Xiao Li, Xiao Luo, ShuHua Zhai, QianShi Wang, Sarp Kerman are with Shanghai Photonic View, Shanghai, 201900, China(email:zuoqin.ding@photonicview.com; xiao.li@photonicview.com; xiao.luo@photonicview.com; gdluckzsh@hotmail.com; qianshi.wang@photonicview.com; sarp.kerman@photonicview.com).

XiuJun Zheng and Zhuo Deng are with Shanghai Industrial µTechnology Research Institute (SITRI), Shanghai, 201800, China(email: xiujun.zheng@ugent.be; chuckdeng@connect.hku.hk).

Bo Wang and He Li are with Shanghai Photonic View, Shanghai, 201900, China and also with State Key Laboratory of Transducer Technology, Shanghai Institute of Microsystem and Information Technology, Chinese Academy of Sciences, 200050, Shanghai, China(email: bowang@mail.sim.ac.cn; lihe314@mail.sim.ac.cn).

Chang Chen is with School of Microelectronics, Shanghai University, Shanghai, 201800, China, Shanghai Photonic View, Shanghai, 201900, China, Shanghai Industrial µTechnology Research Institute (SITRI), Shanghai, 201800, China, State Key Laboratory of Transducer Technology, Shanghai Institute of Microsystem and Information Technology, Chinese Academy of Sciences, 200050, Shanghai, China and Institute of Medical Chips, Ruijin Hospital, Shanghai Jiao Tong University School of Medicine, 200025, Shanghai, China(email: chang.chen@shsmu.edu.cn).

I. INTRODUCTION

OVER recent decades, Photonic Integrated Circuits (PIC) have undergone rapid development, emerging as compelling solutions for the miniaturization and integration of optoelectronic applications. Initially driven by optical communication and interconnect [1], PICs have progressively extended to encompass areas like life sciences [2], LiDAR [3], spectroscopy [4], and quantum photonics [5].

PICs are built on a variety of material platforms, each offering unique advantages and challenges. A single platform cannot cover all possible applications [6]. For example, the Silicon-on-Insulator (SOI) platform [7] has emerged as a mature and commercially viable technology for PICs due to its high refractive index contrast and compatibility with existing complementary metal oxide semiconductor (CMOS) manufacturing processes. However, Si has a narrow bandgap of 1.1 eV [8]. It cannot be used for wavelengths shorter than 1.1 µm. Consequently, the use of SOI in devices operating within the visible range is restricted.

Inspired by the success of the SOI platform, there is growing interest in expanding photonic integration into the visible spectrum as most of the life sciences applications require visible light. Although several materials [9], [10] are transparent in this range, Silicon Nitride (SiN) has stood out as a prime candidate due to its low loss, potential CMOS compatibility, and relatively high refractive index (n~2) [11]. SiN PICs have found wide applications in fields such as super-resolution microscopy [12], biosensing [13], spectroscopy [14], and Optical Coherence Tomography (OCT) [15].

Due to its wide bandgap of 5.1 eV, SiN extends its transparency window down to 400 nm, making it highly suitable for photonic integration across the visible to near-infrared (VIS-NIR) spectrum [8], [16]. Besides, SiN's moderately high refractive index (n~2) not only facilitates an efficient integration of photonic components but also helps reduce propagation losses associated with sidewall roughness compared to Si. Meanwhile, this moderate refractive index contrast implies that the SiN platform has large manufacturing tolerances and does not demand high-precision manufacturing facilities. Moreover, SiN has virtually zero two-photon absorption (TPA) in the communication band, minimizing additional waveguide losses at high power. This is a crucial advantage for high-power applications [17]. Low TPA enables using high power confinement and efficient nonlinear optical processes like Four Wave Mixing (FWM) [18], crucial for applications in optical signal processing and generation.

This work is licensed under a Creative Commons Attribution 4.0 License. For more information, see https://creativecommons.org/licenses/by/4.0/

This article has been accepted for publication in IEEE Photonics Journal. This is the author's version which has not been fully edited and
content may change prior to final publication. Citation information: DOI 10.1109/JPHOT.2024.3467310

Finally, SiN's potential compatibility with the CMOS process makes it flexible for multilayer SiN photonic integration [19] and heterogeneous integration with other platforms such as SOI [20].

SiN platform fabrication process involves common flows in a CMOS line where the waveguide layer can be deposited either by Low-Pressure Chemical Vapor Deposition (LPCVD) or Plasma Enhanced Chemical Vapor Deposition (PECVD). LPCVD provides high-performance and stoichiometric SiN thin films. It was demonstrated that the LPCVD SiN refractive index can be tuned by modifying the gas ratio [21], [22]. However, LPCVD requires high-temperature processing (>700°C). Additionally, LPCVD generates significant internal stress, making thick SiN preparation challenging for thicknesses of more than a few hundred nm [23], [24]. PECVD allows SiN deposition at lower temperatures (<400°C), making it compatible with processing after metal deposition in the back-end of the line (BEOL) and easing the integration capabilities [20]. The refractive index of PECVD-deposited SiN can be adjusted by altering the deposition conditions, producing films that range from silicon-rich (high refractive index) to nitrogen-rich (low refractive index). However, there is significant light absorption at 1520 nm, a critical wavelength for telecommunication, due to the high amount of Si-H and N-H Bonding [25].

As a bridge between foundries and consumers, Process Design Kits (PDKs) play a pivotal role in PIC research and development (R&D). Customers can design their circuits rapidly based on the PDK and make customized components for particular requirements. Several foundries like LioniX Int, IMB-CNM, LIGENTEC, imec, CUMEC, and SITRI have presented available SiN-based photonic integration solutions along with their respective PDKs [7], [26], mainly in O-Band and C-Band. Additionally, there is a growing trend of institutions developing their own SiN PDKs, further expanding the resources available to designers and engineers in the field [27]. However, there are limited PDKs available for the visible range [28], [29], [30].

This paper details our efforts in developing PDKs at VIS-NIR spectrum on the PECVD and LPCVD SiN platform, with thicknesses of 180 nm and 150 nm, respectively. The proposed PDKs are accessible through Shanghai Industrial μTechnology Research Institute (SITRI) 200 mm line. It comprises basic passive photonic components such as waveguides, bends, linear grating couplers (LGC), multimode interference (MMI) couplers, directional couplers (DC), and micro-ring resonators (MRR). First, we defined the fabrication processes and testing methodologies for SiN PIC chips. Then we conducted automated wafer-level measurements to assess the performance of these components and to gain insight into their wafer-level variations. Our results indicate that the fundamental photonic components within the PDK demonstrate low-loss and reliable performance, competitive to other SiN photonics platform providers.

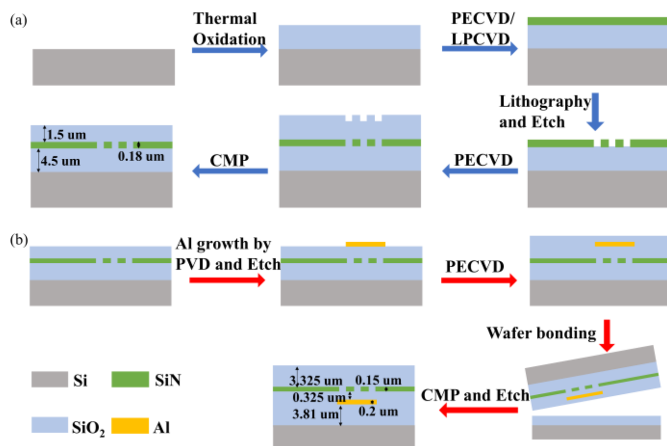

Fig. 1. The fabrication process of PIC chips. (a) The fabrication process of PECVD and LPCVD SiN photonic components; (b) The fabrication process of grating bottom metal layer.

II. Fabrication and Method

We have successfully developed a PDK for the VIS-NIR range utilizing the SiN platform (PECVD and LPCVD). The fabrication of the PIC chips was carried out at the SITRI 200 mm line. The PECVD platform, with a SiN layer thickness of 180 nm, was designed to operate effectively at optical wavelengths of 532 nm, 573 nm, 638 nm, and 673 nm. The LPCVD-based components were targeted for longer wavelengths, specifically 785 nm and 860 nm, with thickness of SiN 150 nm. Here we aimed to keep the sidewall scattering losses low by still using a relatively thin waveguide layer for longer wavelengths. Moreover, the refractive index of LPCVD SiN (~2.03) is higher than PECVD SiN refractive index (~1.88). Additionally, a 200 nm Al layer was placed 325 nm below the LPCVD SiN layer to reflect the transmitted light and diffract it to the waveguide by grating again, thus to enhance LGC efficiency.

The fabrication process for the PECVD SiN platform is shown in Fig. 1(a). The bottom silicon dioxide layer was grown on the silicon substrate by thermal oxidation. Next, a SiN layer of 180 nm film thickness was deposited by PECVD. Photolithography and dry etching steps were performed to transfer the pattern of waveguides and components. The top oxide layer was subsequently deposited by PECVD. Finally, chemical mechanical polishing (CMP) was applied to thin the top layer thickness and smoothen the surface. The complete stack of PECVD platform is illustrated in Fig. 1(a).

The fabrication process for the LPCVD platform was similar to PECVD, except that the SiN film was deposited by LPCVD with a film thickness of 150 nm. The next process steps include the deposition of Al metal film by physical vapor deposition (PVD) and patterning. The stack was subsequently capped with the top oxide layer and then planarized by CMP. Next, the wafer with SiN waveguide and Al reflector was flipped and bonded to a thermo-oxidated silicon wafer as shown in Fig. 1(b). Finally, a combination of CMP and silicon etching was performed to remove the sacrificial silicon substrate.

This work is licensed under a Creative Commons Attribution 4.0 License. For more information, see https://creativecommons.org/licenses/by/4.0/

This article has been accepted for publication in IEEE Photonics Journal. This is the author's version which has not been fully edited and content may change prior to final publication. Citation information: DOI 10.1109/JPHOT.2024.3467310

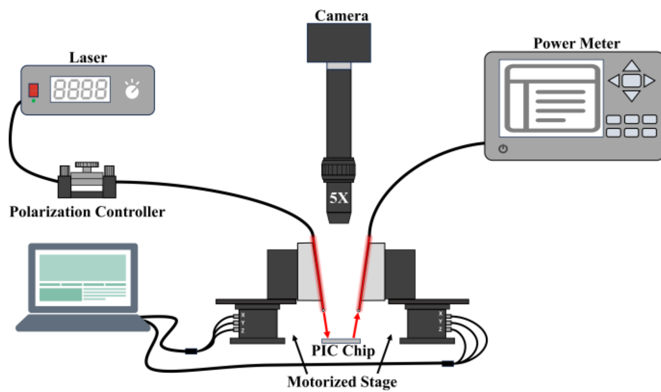

Fig. 2. The prototype of photonic component measurement.

The chips were measured at Photonic View, which provides PIC measurement services from die to wafer level. Various and customized test routines were involved such as manual, semi-automated, and fully-automated tests. In this work, we performed measurements on a single 200 mm wafer from each PECVD and LPCVD platform fabrication lot. A generic illustration of photonic component measurement is displayed in Fig. 2. The PIC chip was fixed on a stage, and input and output optical fibers were attached on motorized stages. A control program was used to drive the motors, enabling quick alignment between fibers and LGCs for rapid automatic measurements. The light from the laser was coupled to the chip via an input fiber, and a fiber polarization controller to ensure TE polarization and maximize the coupling efficiency. The output fiber was connected to an optical power meter to measure the output optical power. A camera positioned above the chip was used to observe the fiber position compared to the photonic components.

III. Passive Photonic Components

A. Waveguide

Waveguides are crucial components in PICs. As shown in Fig. 3(a) and (b), the sidewalls of the fabricated waveguides were not exactly vertical, with angle of ~77 degrees, which was considered in our simulation (Fig. 3(c)). Here we used a finite-difference eigenmode (FDE) solver to analyze waveguide modes. In the case of a ridge waveguide, the high-order modes emerge as the thickness and width of the waveguide increase to a certain value. To ensure the single mode in vertical (y) direction, we first chose the thickness to be 180 nm for the PECVD SiN platform and 150 nm for the LPCVD SiN platform. Then the waveguide width was analyzed to support only fundamental mode. Fig. 3(d) graphically represents how the effective refractive index of TE0 mode and TE1 mode varies with the waveguide width at different wavelengths. For instance, 390 nm waveguide width at 532 nm wavelength allows only the fundamental TE mode.

Due to fabrication variations, we applied a margin of about 10% to pick the waveguide width of each wavelength. The waveguides were fabricated according to the parameters in corresponding platforms as described in Table I. Fig. 3(b) displays the SEM image of the waveguide fabricated in the

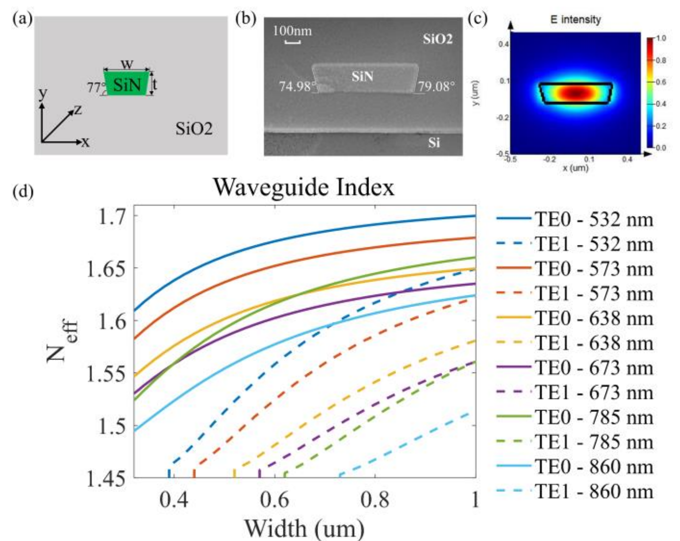

Fig. 3. Simulation results of the waveguides. (a) The cross section of the ridge waveguide; (b) The SEM image of waveguide cross section; (c) The field amplitude profile of the waveguide; (d) Effective refractive index versus waveguide width at different wavelengths and platforms.

TABLE I

The Waveguide Sizes for Different Wavelengths

Wavelength (nm)	Platform	Thickness (nm)	Width (nm)
532	PECVD	180	360
573	PECVD	180	410
638	PECVD	180	470
673	PECVD	180	510
785	LPCVD	150	560
860	LPCVD	150	560

LPCVD platform. The sizes match the designed values, with sidewall angles of ~77±2°. Fig. 3(c) illustrates its field profile, confirming that the light is effectively confined within the SiN waveguide.

We conducted tests on the output power of spiral lines with varying lengths (as illustrated in Fig. 4(a)), and calculated the propagation loss of the waveguide using cutback method. The waveguide loss measurements for both platforms at different wavelengths were conducted for one whole wafer (45 reticles) and the results are depicted in Fig. 4(b). In the VIS-NIR range, the propagation loss decreases as the wavelength increases, which is linked to the decreasing mode overlap at the sidewalls and decreasing SiN absorption coefficient with increasing wavelengths. Low propagation loss (<1dB/cm) was achieved with wavelengths above 638 nm. Furthermore, the wafer-level measurements for the 860 nm waveguide loss are detailed in Fig. 4(c). These results show a remarkably low propagation loss of 0.34 ± 0.04 dB/cm, demonstrating not only low loss but also excellent uniformity across the wafer.

Table II summarizes the loss of reported SiN waveguide propagation losses in recent literature, from 405 nm to 850 nm. In the literature, the SiN waveguide loss was reported as >6 dB/cm around 400 nm. As for over 600 nm, the reported losses vary between 0.26~3.6 dB/cm. In comparison, we report a waveguide loss with excellent performance (<1dB/cm between 638 nm and 860 nm). For over 800 nm, our loss was considerably smaller than other work[31]. Corato-Zanarella et al. [32] demonstrated the state-of-the-art in SiN waveguide

This work is licensed under a Creative Commons Attribution 4.0 License. For more information, see https://creativecommons.org/licenses/by/4.0/

This article has been accepted for publication in IEEE Photonics Journal. This is the author's version which has not been fully edited and content may change prior to final publication. Citation information: DOI 10.1109/JPHOT.2024.3467310

TABLE II
THE PROPAGATION LOSS FOR SiN WAVEGUIDES IN THE VIS~NIR SPECTRUM

ref	Wavelength (nm)	Platform	Polarization	Thickness (nm)	Width (nm)	Confinement factor	Loss (dB/cm)
[28]	466~550 552~648	PECVD	TM TE	135	340 520	~0.446@466nm 0.371 @648nm	2.8~1.5 1.9~1.1
[31]	450~850	LPCVD	TE	150	800	/	6.85~0.59
[32]	461~785	LPCVD	TE	275	4000	/	2.4~0.036
[33]	405~640	PECVD	TE TM	150	380~520	/	7.1~2.2 6.7~1.8
[34]	458~634 634	LPCVD PECVD	TE	100	250~500 500	/	6.01~0.26 1.15
[35]	532 638	PECVD	/	180 220	350 340	0.715 0.651	1.6 0.87
[36]	633	LPCVD	TE	400	400	0.905	3.6
[37]	660	LPCVD	TE	320	1000	0.979	1.7
This work	532~673 785~860	PECVD LPCVD	TE	180 150	360~510 560	0.731~0.628 0.540~0.469	2.5~0.8 0.55~0.34

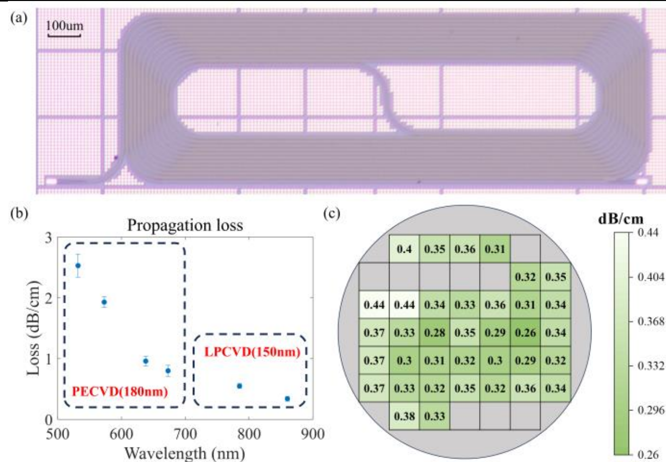

Fig. 4. Propagation loss of waveguides. (a) The structure for waveguide propagation loss characterization: spiral line; (b) Propagation loss of waveguides at different wavelengths; (c) Wafer-Level measurement waveguide loss at 860 nm.

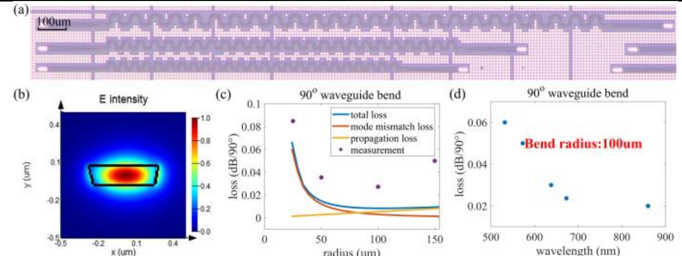

Fig. 5. The loss of bend waveguide. (a) The structure for bend waveguides characterization; (b) Field profile of 90° waveguide bend at 860 nm with radius 20 μm; (c) The loss of 90° waveguide bend versus radius at 860 nm; (d) Measured results of bend waveguides at different wavelengths.

loss across the visible spectrum with an ultra-low loss waveguide of 0.036 dB/cm at 780 nm by increasing the waveguide width beyond the single-mode condition (expanded waveguide). Expanded waveguides are useful to decrease propagation losses caused by sidewall scattering at the cost of low packing density and the risk of coupling into higher-order modes due to fabrication imperfections. Our work focuses on single-mode waveguides with small cross-sections and high density. These results show that our work is comparable to the reported SiN losses across VIS- NIR spectrum.

B. 90° bend

90° waveguide bend is a common and important component for routing. The bend radius of waveguides is a crucial factor for achieving the high-density integration of photonic components. A smaller bend radius allows a more compact design, enabling the integration of a greater number of components within limited footprints[38].

The losses associated with 90° waveguide bends are categorized into three primary types: propagation loss, radiation loss, and mode mismatch loss. The radiation loss is much smaller than the other two and can be ignored for large radius (tens of um). Therefore, we focused on the propagation loss and mode mismatch loss for varying bend radius, as shown in Fig. 5(c). The propagation loss was calculated based on the test results presented in 3.1 and the mode mismatch loss was obtained from the FDE solver. Mode mismatch loss occurs due to the differences between the mode field profiles of bend and straight waveguides. When the bend radius is small, the difference between the field profiles of bend and straight waveguides is large, resulting in particularly significant mode mismatch loss. As the bend radius increases, the mode profile in the bend becomes more similar to that in a straight waveguide, reducing the mode mismatch loss. Consequently, when the radius is sufficiently large, the mode mismatch loss becomes negligible, and the propagation loss dominates the total loss. However, increasing the bend radius to reduce the mode mismatch and the radiation losses comes at the cost of increased footprint, which limits the density of photonic integration. Therefore, a trade-off between loss and compact integration is necessary to determine the optimal bend radius.

C. Linear grating coupler

Grating couplers are commonly used to efficiently couple light between waveguides and fibers. They diffract the input light from an optical fiber that is vertical to the chip surface into waveguides. This feature enables a flexible arrangement of optical input/output (I/O) ports anywhere on the chip, which promotes high levels of optical component integration. Additionally, grating couplers offer better alignment tolerance

This work is licensed under a Creative Commons Attribution 4.0 License. For more information, see https://creativecommons.org/licenses/by/4.0/

This article has been accepted for publication in IEEE Photonics Journal. This is the author's version which has not been fully edited and
content may change prior to final publication. Citation information: DOI 10.1109/JPHOT.2024.3467310

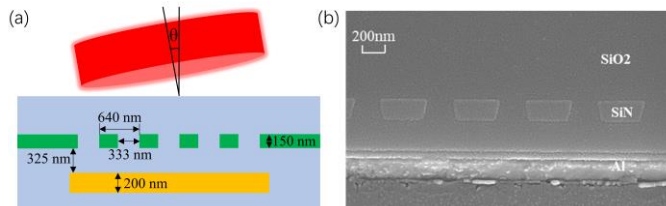

Fig. 6. The structure of LGC. (a) The structure of LGC at 860 nm. (b) The SEM image of LGC with a metal layer.

TABLE III
MEASUREMENT RESULTS OF LGC AT DIFFERENT WAVELENGTHS

Wavelength (nm)	Platform	With a Metal Layer	Loss (dB)	Number of chips
532	PECVD	NO	9.6+-1	32
638	PECVD	NO	7.0+-0.27	45
785	LPCVD	YES	2.6+0.07	8
860	LPCVD	YES	3.2+-0.24	6

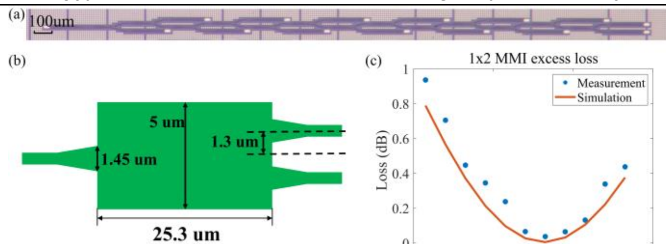

Fig. 7. The Measurement results of 1x2 MMI. (a) Structure of cascaded MMI for measurement; (b) The structure of 1×2 MMI at 860 nm; (c) 1×2 MMI excess loss at 860 nm.

compared to edge coupling in general, enabling wafer-level testing of chips and facilitating both testing and packaging processes. Adding a metal reflector layer[39] or distributing Bragg reflectors[40] below a grating coupler can reflect the transmitted light and diffract it to the waveguide by grating again, thus to enhance efficiency.

Fig. 6(a) illustrates the structure of LGC at 860 nm. The fiber tilt angle (θ) is 10° to ensure high coupling efficiency. The period (Λ) and etching width (w_e) of LGC were optimized to be 640 nm and 333 nm, respectively, with a duty cycle (DC) of 0.52 (DC=w_e/Λ). In order to improve the grating efficiency, a metal layer was added at the bottom of the grating with a gap of 325 nm. The distance was kept small to reduce the loss variation caused by the thickness deviation of the underlying silicon dioxide. The SEM image of LGC is shown in Fig. 6(b), indicating a sidewall angle same as the waveguide etch.

Table III shows the LGC losses and the number of measured reticles at various wavelengths. Specifically, the LGC loss at 532 nm was around 9.6 dB by fully-automated tests and about 6.4 dB by manual test, indicating that a better position for alignment can be found manually. For short wavelength, the coupling efficiency is sensitive to the fiber-to-grating alignment which possibly caused a systematic error in the case of fully automated setup. For wavelength 638 nm, the loss was around 7 dB. The losses measured at 785 nm and 860 nm were 2.6 dB and 3.2 dB, significantly lower than the other wavelengths thanks to the metal layer. It is also estimated by simulations that the losses at 532 nm and 638 nm can be improved to 2.1 dB by adding bottom metal.

TABLE IV
MMI PERFORMANCES AT DIFFERENT WAVELENGTHS

MMI	Wave-length (nm)	MMI length (um)	MMI width (um)	Excess loss (dB)	Imbalance (dB)	Number of chips
1×2	532	38.07	5	0.13+-0.08	22.9+-5.3	45
1×2	573	36.88	5	0.26+-0.07	20.9+-5.6	45
1×2	638	32.37	5	0.08+-0.09	20.9+-3.8	42
1×2	673	31.11	5	0.16+-0.04	17.8+-3.6	45
1×2	785	27.50	5	0.08+-0.01	23.9+-5.4	4
1×2	860	25.30	5	0.03+-0.01	28.2+-8.8	4

D. Power splitter

1) *Multimode interference coupler*

1×2 MMI is a conventional 3 dB beam splitter, which works by the self-imaging effect. Within an MMI, a multimode waveguide allows multiple modes to propagate simultaneously. These modes interfere with each other, leading to the periodic generation of one or more images of the input mode field along the transmission direction. The splitting occurs at specific locations known as self-imaging points. By strategically positioning output waveguides at these points, the input beam can be evenly split into two or more output beams. It provides advantages compared to directional couplers such as large manufacturing tolerance and wavelength-insensitive splitting ratios.

The structure of 1×2 MMI at 860 nm is depicted in Fig. 7(b). We defined the MMI width as 5 μm to limit the footprint without compromising the performance. Based on the width, we optimized the MMI length, taper width, and offset to 25.3 μm, 1.45 μm, and 1.3 μm for 860 nm, respectively. We cascaded multiple 1×2 MMI structures (Fig. 7(a)) and measured the output power at each level, then used the cutback method to obtain the excess loss and imbalance. The imbalance is defined as $-10\log\left|\frac{P_1-P_2}{P_0}\right|$, where P0 is the input power, P_1 and P_2 are the two output powers. Fig. 7(c) illustrates the measurement results of 1×2 MMI at 860 nm. The minimum excess loss appears at 25.3 μm MMI length, which matched accurately with our simulation results. The minimum excess loss and imbalance were 0.03 dB and 28.2 dB, respectively. Furthermore, we have designed and characterized the 1×2 MMI at wavelengths 532 nm, 573 nm, 638 nm, 673 nm, and 785 nm. The measured results number of measured reticles are summarized in Table IV. Some of those wavelengths exhibited relatively higher loss due to a mismatch between the expected SiN refractive index and the fabricated one.

2) *Directional coupler*

The structure of DC at 860 nm is shown in Fig. 8(b). It consists of two single-mode waveguides placed near each other between the symmetric and anti-symmetric modes. The gap between the waveguides was set at 0.3 μm. Various coupling lengths were designed to achieve different splitting ratios (5.6 μm for 1:1 splitting ratio). The S-bend waveguides on the sides were used to connect the DC with other components.

Similar to MMI, a cascaded structure (Fig. 8(a)) was used to measure the performance of DCs at 860 nm. The

This work is licensed under a Creative Commons Attribution 4.0 License. For more information, see https://creativecommons.org/licenses/by/4.0/

This article has been accepted for publication in IEEE Photonics Journal. This is the author's version which has not been fully edited and
content may change prior to final publication. Citation information: DOI 10.1109/JPHOT.2024.3467310

measurement results are shown in Fig. 8(c). As the length of

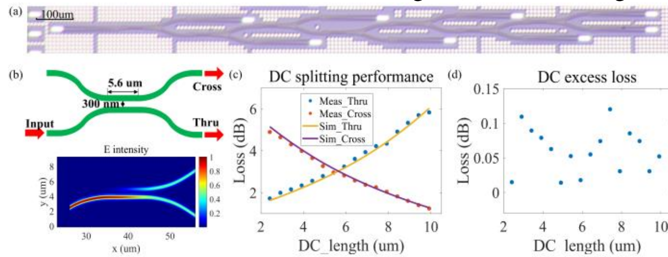

Fig. 8. The measurement results of DC at 860 nm. (a) Structure of cascaded DC for measurement; (b) The schematic of DC at 860 nm and field profile at 1:1 splitting; (c) DC splitting performance versus length at 860 nm; (d) DC excess loss versus length at 860 nm.

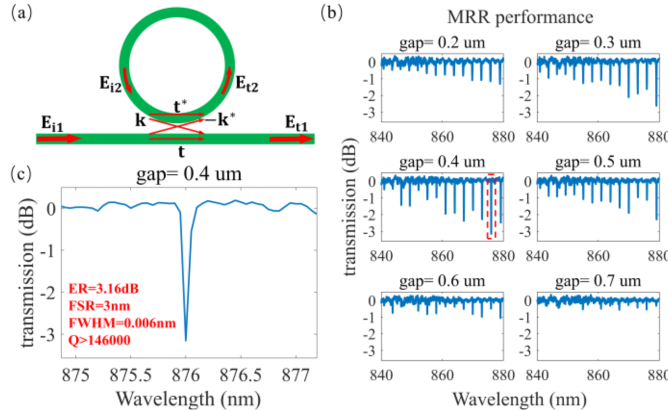

Fig. 9. MRR transmission. (a) The straight-through MRR structure; (b) Transmission measurement results of MRR with different gaps; (c) Amplified image around 876 nm for MRR with a radius of 21 μm from Fig. 9(b).

the coupling region increases, there is a corresponding increase in the amount of light that is transferred to the adjacent waveguide within the range we designed and tested. DCs with different coupling lengths can realize different splitting ratios. 3 dB splitting ratio was successfully realized when the DC length was around 5.5 μm, with an excess loss of <0.1dB (Fig. 8(d)). The coupling length is very close to the designed value of 5.64 um, indicating small fabrication deviations.

E. Micro Ring resonator

MRR consists of a straight waveguide coupled with a micro-ring situated nearby. This configuration leverages the phenomenon of evanescent field coupling between the straight waveguide and the ring. The wavelength that meets phase-matching conditions will oscillate within the ring.

We demonstrated a straight-through MRR (Fig. 9(a)) with high quality (Q) factor around 860 nm wavelength. The width of the ring and bus waveguide is 600 nm to reduce the bending loss as well as ensure single mode condition. The radius was chosen as 21 μm for small footprint. MRRs with gaps ranging from 200 nm to 700 nm were fabricated and tested. Our results, illustrated in Fig. 9(b), indicate that the critical coupling occurs when the gap is about 400 nm. The FSR of the resonance is approximately 3 nm which matches the expected value. The fitting full width at half maximum (FWHM) is 0.006 nm and the calculated Q factor is 146000. The Q factor corresponds to the loss of ~2.1 dB/cm, which mainly comes from the bending loss and the propagation loss. For the 21 um-radius, the simulated bending loss is about 1.6 dB/cm at 876 nm. If we use MRR with larger radius thus lower bending loss, the Q factor will further increase.

V. Conclusion

In this paper, we present our progress in PDK development for the SITRI 200mm SiN photonics line. The proposed PDKs feature a comprehensive library of passive components designed on two SiN platforms, with thicknesses of 180 nm for PECVD and 150 nm for LPCVD. Our measurements across the wavelength range from 532 nm to 860 nm indicate low propagation losses, ranging from 2.5 dB/cm to 0.34 dB/cm. Additionally, we successfully demonstrated bend losses of <0.06 dB per 90° bend for a radius of 100 μm at various wavelengths. For the PECVD platform, the LGC losses were approximately 6.5 dB at 532 nm and 638 nm. This was significantly improved to 2.6 dB and 3.2 dB at 785 nm and 860 nm by incorporating a metal layer on the LPCVD platform. It is estimated by FDTD simulations that the LGCs at 532 nm and 638 nm can be improved to 2.1 dB in the same way. Moreover, we developed low excess loss beam splitters, achieving <0.1 dB loss via 1×2 MMI, alongside demonstrating a DC capable of achieving any desired splitting ratio with minimal loss. Also, an MRR with a high Q factor of 146000 at 860 nm was demonstrated thanks to the low waveguide loss. Apart from what was mentioned in this article, we designed a set of 2×2 MMIs and a polarization-handling device that can rotate the input TM0 mode to TE1 mode and then convert the TE1 mode to TE0 by an asymmetrical directional coupler. The optimized polarization rotator-beam splitter (PRBS) shows a high TM0 to TE0 conversion efficiency of <0.75 dB in 120 nm bandwidth and high fabrication tolerance, which will be fabricated and characterized in the future.

The SITRI 200 mm line supports photonic integrations of multiple optical functionalities, including optical transceivers, optical computing, and optical sensing. They provide PDKs for their SOI platform, as well as multi-project wafer (MPW) services. Here, we presented our results on a PDK developed for the VIS-NIR range in SITRI's 200 mm SiN photonics line. The proposed PDK presents high-performance and reliable passive components for the VIS-NIR range. We believe that our PDK is going to be useful for researchers and companies that would like to pursue development in SITRI's 200 mm SiN photonics line for VIS-NIR wavelengths.

Acknowledgment

This work is supported by the testing team at Shanghai Photonic View led by Dr. Shuhua Zhai, including Zhengping Bao, Jian Duan, Jianxin Gao, Di Ji, Xiangyue Xiao and Jiain Zhu, the PIE team at SITRI led by Prof. Mingbin Yu, Dr. Wei Wang, Dr. Baiyin Wang, and PIE team at Shanghai Photonic View, Mr. Laisheng He, Dr. Xiangwei Meng.

This work is licensed under a Creative Commons Attribution 4.0 License. For more information, see https://creativecommons.org/licenses/by/4.0/

This article has been accepted for publication in IEEE Photonics Journal. This is the author's version which has not been fully edited and content may change prior to final publication. Citation information: DOI 10.1109/JPHOT.2024.3467310

REFERENCES

[1] F. Kish *et al.*, "System-on-Chip Photonic Integrated Circuits," *Ieee Journal of Selected Topics in Quantum Electronics,* vol. 24, no. 1, pp. 1-20, Jan-Feb 2018, Art no. 6100120, doi: 10.1109/jstqe.2017.2717863.

[2] D. Ozcelik, H. Cai, K. D. Leake, A. R. Hawkins, and H. Schmidt, "Optofluidic bioanalysis: fundamentals and applications," *Nanophotonics,* vol. 6, no. 4, pp. 647-661, Jul 2017, doi: 10.1515/nanoph-2016-0156.

[3] I. Kim *et al.*, "Nanophotonics for light detection and ranging technology," *Nature Nanotechnology,* vol. 16, no. 5, pp. 508-524, May 2021, doi: 10.1038/s41565-021-00895-3.

[4] Y. Chen, H. T. Lin, J. J. Hu, and M. Li, "Heterogeneously Integrated Silicon Photonics for the Mid-Infrared and Spectroscopic Sensing," *Acs Nano,* vol. 8, no. 7, pp. 6955-6961, Jul 2014, doi: 10.1021/nn501765k.

[5] J. H. Kim, S. Aghaeimeibodi, J. Carolan, D. Englund, and E. Waks, "Hybrid integration methods for on-chip quantum photonics," *Optica,* vol. 7, no. 4, pp. 291-308, Apr 2020, doi: 10.1364/optica.384118.

[6] P. Kaur, A. Boes, G. H. Ren, T. G. Nguyen, G. Roelkens, and A. Mitchell, "Hybrid and heterogeneous photonic integration," *Apl Photonics,* vol. 6, no. 6, p. 061102, Jun 2021, Art no. 061102, doi: 10.1063/5.0052700.

[7] S. Y. Siew *et al.*, "Review of Silicon Photonics Technology and Platform Development," *Journal of Lightwave Technology,* vol. 39, no. 13, pp. 4374-4389, Jul 2021, doi: 10.1109/jlt.2021.3066203.

[8] R. Soref, "Mid-infrared photonics in silicon and germanium," *Nature Photonics,* vol. 4, no. 8, pp. 495-497, Aug 2010, doi: 10.1038/nphoton.2010.171.

[9] M. M. Aslan *et al.*, "Low-loss optical waveguides for the near ultra-violet and visible spectral regions with Al_2O_3 thin films from atomic layer deposition," *Thin Solid Films,* vol. 518, no. 17, pp. 4935-4940, Jun 2010, doi: 10.1016/j.tsf.2010.03.011.

[10] T.-J. Lu *et al.*, "Aluminum nitride integrated photonics platform for the ultraviolet to visible spectrum," *Optics Express,* Article vol. 26, no. 9, pp. 11147-11160, Apr 30 2018, doi: 10.1364/oe.26.011147.

[11] F. Gardes *et al.*, "A Review of Capabilities and Scope for Hybrid Integration Offered by Silicon-Nitride-Based Photonic Integrated Circuits," *Sensors,* vol. 22, no. 11, Jun 2022, Art no. 4227, doi: 10.3390/s22114227.

[12] R. Diekmann *et al.*, "Chip-based wide field-of-view nanoscopy," *Nature Photonics,* Article vol. 11, no. 5, pp. 322-328, May 2017, doi: 10.1038/nphoton.2017.55.

[13] H. Altug, S.-H. Oh, S. A. Maier, and J. Homola, "Advances and applications of nanophotonic biosensors," *Nature Nanotechnology,* Review vol. 17, no. 1, pp. 5-16, Jan 2022, doi: 10.1038/s41565-021-01045-5.

[14] Z. Yang, T. Albrow-Owen, W. Cai, and T. Hasan, "Miniaturization of optical spectrometers," *Science,* Review vol. 371, no. 6528, pp. 480-+, Jan 29 2021, Art no. eabe0722, doi: 10.1126/science.abe0722.

[15] G. Yurtsever, N. Weiss, J. Kalkman, T. G. van Leeuwen, and R. Baets, "Ultra-compact silicon photonic integrated interferometer for swept-source optical coherence tomography," *Optics Letters,* Article vol. 39, no. 17, pp. 5228-5231, Sep 1 2014, doi: 10.1364/ol.39.005228.

[16] P. Munoz *et al.*, "Foundry Developments Toward Silicon Nitride Photonics From Visible to the Mid-Infrared," *Ieee Journal of Selected Topics in Quantum Electronics,* Article vol. 25, no. 5, pp. 1-13, Sep-Oct 2019, Art no. 8200513, doi: 10.1109/jstqe.2019.2902903.

[17] T. K. Liang and H. K. Tsang, "Nonlinear absorption and Raman scattering in silicon-on-insulator optical waveguides," *Ieee Journal of Selected Topics in Quantum Electronics,* Article vol. 10, no. 5, pp. 1149-1153, Sep-Oct 2004, doi: 10.1109/jstqe.2004.835290.

[18] D. J. Moss, R. Morandotti, A. L. Gaeta, and M. Lipson, "New CMOS-compatible platforms based on silicon nitride and Hydex for nonlinear optics," *Nature Photonics,* Review vol. 7, no. 8, pp. 597-607, Aug 2013, doi: 10.1038/nphoton.2013.183.

[19] K. Shang, S. Pathak, B. Guan, G. Liu, and S. J. B. Yoo, "Low-loss compact multilayer silicon nitride platform for 3D photonic integrated circuits," *Optics Express,* Article vol. 23, no. 16, pp. 21334-21342, Aug 10 2015, doi: 10.1364/oe.23.021334.

[20] W. D. Sacher *et al.*, "Monolithically Integrated Multilayer Silicon Nitride-on-Silicon Waveguide Platforms for 3-D Photonic Circuits and Devices," *Proceedings of the Ieee,* Article vol. 106, no. 12, pp. 2232-2245, Dec 2018, doi: 10.1109/jproc.2018.2860994.

[21] M. Blasco, S. Dacunha, C. Dominguez, and J. Faneca, "Silicon nitride stoichiometry tuning for visible photonic integrated components," *Applied Physics Letters,* Article vol. 124, no. 22, May 27 2024, Art no. 221104, doi: 10.1063/5.0204582.

[22] C. J. Krückel, A. Fülöp, Z. C. Ye, P. A. Andrekson, and V. Torres-Company, "Optical bandgap engineering in nonlinear silicon nitride waveguides," *Optics Express,* vol. 25, no. 13, pp. 15370-15380, Jun 2017, doi: 10.1364/oe.25.015370.

[23] J. S. Levy, A. Gondarenko, M. A. Foster, A. C. Turner-Foster, A. L. Gaeta, and M. Lipson, "CMOS-compatible multiple-wavelength oscillator for on-chip optical interconnects," *Nature Photonics,* Article vol. 4, no. 1, pp. 37-40, Jan 10 2010, doi: 10.1038/nphoton.2009.259.

[24] M. H. P. Pfeiffer *et al.*, "Photonic Damascene process for integrated high-Q microresonator based nonlinear photonics," *Optica,* Article vol. 3, no. 1, pp. 20-25, Jan 20 2016, doi: 10.1364/optica.3.000020.

[25] R. M. de Ridder, K. Wörhoff, A. Driessen, P. V. Lambeck, and H. Albers, "Silicon oxynitride planar waveguiding structures for application in optical communication," *Ieee Journal of Selected Topics in Quantum Electronics,* Article vol. 4, no. 6, pp. 930-937, Nov-Dec 1998, doi: 10.1109/2944.736079.

[26] C. Xiang, W. Jin, and J. E. Bowers, "Silicon nitride passive and active photonic integrated circuits: trends and prospects," *Photonics Research,* Review vol. 10, no. 6, pp. A82-A96, Jun 1 2022, doi: 10.1364/prj.452936.

[27] C. McDonough *et al.*, "AIM Photonics Demonstration of a 300 mm Si Photonics Interposer," in *IEEE 73rd Electronic Components and Technology Conference (ECTC)*, Orlando, FL, 2023, in Electronic Components and Technology Conference, 2023, pp. 233-238.

[28] W. D. Sacher *et al.*, "Visible-light silicon nitride waveguide devices and implantable neurophotonic probes on thinned 200 mm silicon wafers," *Optics Express,* Article vol. 27, no. 26, pp. 37400-37418, Dec 23 2019, doi: 10.1364/oe.27.037400.

[29] A. Z. Subramanian *et al.*, "Low-Loss Singlemode PECVD Silicon Nitride Photonic Wire Waveguides for 532-900 nm Wavelength Window Fabricated Within a CMOS Pilot Line," *Ieee Photonics Journal,* Article vol. 5, no. 6, Dec 2013, Art no. 2202809, doi: 10.1109/jphot.2013.2292698.

[30] D. Geuzebroek, A. van Rees, E. Klein, K. Lawniczuk, and Ieee, "Ultra-wide Band (400-1700nm) Integrated Spectrometer based on Arrayed Waveguide Gratings for Spectral Tissue Sensing," in *14th IEEE International Conference on Group IV Photonics (GFP)*, Berlin, GERMANY, 2017, in IEEE International Conference on Group IV Photonics, 2017, pp. 79-80.

[31] J. A. Smith, H. Francis, G. Navickaite, and M. J. Strain, "SiN foundry platform for high performance visible light integrated photonics," *Optical Materials Express,* Article vol. 13, no. 2, pp. 458-468, Feb 1 2023, doi: 10.1364/ome.479871.

[32] M. Corato-Zanarella, X. Ji, A. Mohanty, and M. Lipson, "Absorption and scattering limits of silicon nitride integrated photonics in the visible spectrum," *Optics Express,* vol. 32, no. 4, pp. 5718-5728, 2024/02/12 2024, doi: 10.1364/OE.505892.

[33] Y. D. Lin *et al.*, "Low-loss broadband bi-layer edge couplers for visible light," *Optics Express,* vol. 29, no. 21, pp. 34565-34576, Oct 2021, doi: 10.1364/oe.435669.

[34] C. Sorace-Agaskar *et al.*, "Versatile Silicon Nitride and Alumina Integrated Photonic Platforms for the Ultraviolet to Short-Wave Infrared," *Ieee Journal of Selected Topics in Quantum Electronics,* vol. 25, no. 5, Sep-Oct 2019, Art no. 8201515, doi: 10.1109/jstqe.2019.2904443.

[35] J. H. Song *et al.*, "Grating devices on a silicon nitride technology platform for visible light applications," *OSA Continuum,* vol. 2, no. 4, pp. 1155-1165, 2019/04/15 2019, doi: 10.1364/OSAC.2.001155.

[36] B.-S. Marcal *et al.*, "Silicon nitride building blocks in the visible range of the spectrum," *Journal of Lightwave Technology,* pp. 1-10, 2024, doi: DOI 10.1109/JLT.2024.3404639.

[37] M. Lelit *et al.*, "Passive Photonic Integrated Circuits Elements Fabricated on a Silicon Nitride Platform," *Materials,* vol. 15, no. 4, Feb 2022, Art no. 1398, doi: 10.3390/ma15041398.

[38] A. Rahim *et al.*, "Expanding the Silicon Photonics Portfolio With Silicon Nitride Photonic Integrated Circuits," *Journal of Lightwave Technology,* Article; Proceedings Paper vol. 35, no. 4, pp. 639-649, Feb 15 2017, doi: 10.1109/jlt.2016.2617624.

[39] S. Romero-Garcia, F. Merget, F. Zhong, H. Finkelstein, and J. Witzens, "Visible wavelength silicon nitride focusing grating coupler with

This work is licensed under a Creative Commons Attribution 4.0 License. For more information, see https://creativecommons.org/licenses/by/4.0/

This article has been accepted for publication in IEEE Photonics Journal. This is the author's version which has not been fully edited and content may change prior to final publication. Citation information: DOI 10.1109/JPHOT.2024.3467310

AlCu/TiN reflector," *Optics Letters,* Article vol. 38, no. 14, pp. 2521-2523, Jul 15 2013, doi: 10.1364/ol.38.002521.

[40] H. Zhang *et al.*, "Efficient silicon nitride grating coupler with distributed Bragg reflectors," *Optics Express,* Article vol. 22, no. 18, pp. 21800-21805, Sep 8 2014, doi: 10.1364/oe.22.021800.

This work is licensed under a Creative Commons Attribution 4.0 License. For more information, see https://creativecommons.org/licenses/by/4.0/